The program LISE: a simulation of fragment separators

D. Bazin[a,*], O. Tarasov[b,c], M. Lewitowicz[c], O. Sorlin[d]

[a] *National Superconducting Cyclotron Laboratory, Michigan State University, East Lansing, MI 48824-1321, USA*
[b] *Flerov Laboratory of Nuclear Reactions, Joint Institute for Nuclear Research, 141980 Dubna, Moscow region, Russia*
[c] *Grand Accélérateur National d'Ions Lourds, BP 55027, 14076 Caen Cedex, France*
[d] *Institut de Physique Nucléaire, BP 1, 91406 Orsay Cedex, France*

Abstract

This paper describes the program LISE which simulates the operation of fragment separators used to produce radioactive beams via fragmentation. Various aspects of the physical phenomena involved in the production of such radioactive beams are discussed. They include fragmentation cross-sections, energy losses in materials, ionic charge-state distributions, as well as ion optics calculations and acceptance effects. This program is highly user-friendly, and is designed not only to forecast intensities and purities for planning future experiments, but also for beam tuning during experiments where its results can be quickly compared to on-line data. In addition, several general-purpose tools such as a physical parameters calculator, a database of nuclear properties, and relativistic two-body kinematics calculations make it useful even for experiments with stable beams. After a general description of fragment separators, the principles underlying the calculations are presented, followed by a practical description of the program and its features. Finally, a few examples of calculations are compared to on-line data, both qualitatively and quantitatively. © 2002 Elsevier Science B.V. All rights reserved.

1. Introduction

1.1. History

The concept of the program LISE was elaborated during the first experiments performed on the fragment separator LISE [1] in the mid-1980s. The aim of these experiments was the production of light drip-line nuclei never observed before. The method of production was the then newly applied projectile fragmentation, in which nuclei accelerated to energies several times above the Coulomb barrier randomly breakup on a fixed target. The kinematic focussing resulting from the high energy of the projectiles provided enhanced yields near zero degrees. The resulting fragments were then collected in a solid angle centered on 0° and separated according to magnetic rigidity by means of two dipoles, so that drip-line nuclei would be observed in the focal plane. The program arose from the need to predict the magnetic rigidity at

*Corresponding author.

  E-mail address: bazin@nscl.msu.edu (D. Bazin).

which a specific fragment would be observed. These calculations had to simulate not only the conditions of the experiment (beam energy, target thickness, etc.), but also the fragmentation process itself. It was quickly realized that such a tool should be highly interactive, so that immediate results from the calculations could be compared to data acquired on-line.

As new and improved methods of selecting the interesting fragments were invented, the program LISE evolved accordingly. The two most important steps were the addition of further fragment selection by energy loss in a wedge-shaped material, and the use of a velocity filter, later followed by a small dipole to compensate for the dispersion and hence obtain mass separation. The resulting secondary beam of fragments could then be made nearly 100% pure, at least for light nuclei ($A < 20$). The term radioactive nuclear beam (RNB) was coined to designate such beams, and a wide range of new experiments to study nuclear matter far from stability became possible.

1.2. Purpose

Projectile fragmentation is now used worldwide in many laboratories to produce RNBs. The ability to predict as well as identify on-line the composition of RNBs is therefore of prime importance. This has shaped the main functions of the program:

- to predict the fragment separator settings necessary to obtain a specific RNB;
- to predict the intensity and purity of the chosen RNB;
- to simulate identification plots for on-line comparison;
- to provide a highly user-friendly graphical environment;
- to allow configuration for different fragment separators.

One of the emphases in the design of the program was that it be easy to learn, so that new users could get results for a prospective experiment very quickly. At the time the program was conceived, this requirement seemed to point towards the use of personal computers, which had then only recently become available.

1.3. Platform

The deliberate choice of personal computers (PCs) to implement the program was made for two reasons:

- to make use of user-friendly features (menus, etc.);
- so that the program could be used in different laboratories worldwide without modification.

One of the drawbacks of this choice was the computing speed (CPU speed), but now the CPU speed of PCs has become comparable to that of mainframe computers. The first versions of the program LISE were written for the Disk Operating System (DOS) of Microsoft[TM] in the language $C++$. It has since been transported to the Windows[TM] environment, which is the platform of version 4.11. With the advent of the World Wide Web, it has become very easy to maintain and update the program, and it can now be freely downloaded from the following internet addresses: www.nscl.msu.edu/lise, dnr080.jinr.ru/lise.html or www.ganil.fr/LISE/proglise.html.

2. General description of fragment separators

While existing dipole-based fragment separators have different characteristics such as acceptances and maximum rigidities, they are all built on the same principles and are run in basically the same way. In many cases, the purpose of these devices is the production of RNBs as intense and pure as possible. However, some experiments can take advantage of having a RNB composed of several different nuclei which can then be studied simultaneously. For these reasons most fragment separators have to accomplish the following:

- filter the nuclei of interest from other fragments;
- collect as many nuclei of interest as possible;
- produce an achromatic image of the primary beam spot for further transport through other beam lines when a RNB is required.
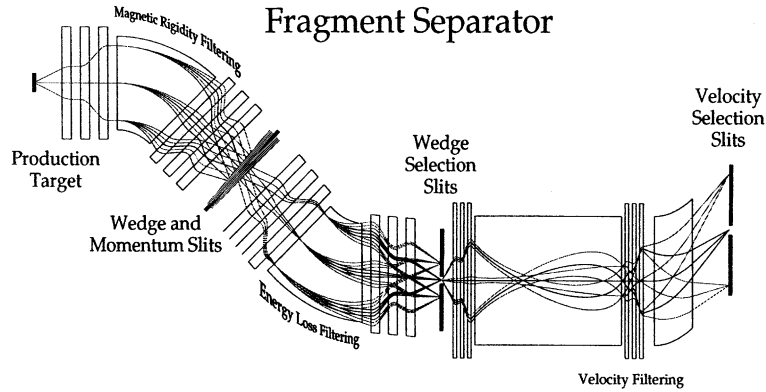
Fragment Separator

Fig. 1. Schematic of a dipole-based fragment separator. The first section runs from the production target to the wedge energy-loss absorber and momentum slits, which set the momentum acceptance. The fragments selected in magnetic rigidity are then refocussed on the wedge selection slits by the second section. Finally, an optional third section provides an additional selection by using a velocity filter before the fragments are sent to a detection system, a reaction target or further beamlines.

A dipole-based fragment separator is generally composed of two momentum-dispersive sections which mirror each other (see Fig. 1). The symmetry point between the two sections is used as a dispersive focal plane, where slits can be used to set the momentum acceptance. In achromatic mode, the second section merely compensates for the dispersion caused by the first, and a one-to-one image of the beam on target can be obtained at the final focus. Because of the nuclear reactions necessary to produce the fragments of interest and straggling in the production target, the emittance of RNBs is usually much greater than that of primary beams. In fact, in most cases the acceptances of the separator elements are completely filled. As a result, transmission losses often occur in the beamlines transporting the RNBs. Many RNBs can be produced using the two first filtering methods described in the following sections. However, depending on the mass region of interest, the nuclei involved, and the goal of the experiment, some RNBs will need further purification using a velocity filter.

2.1. Magnetic-rigidity filtering

The first stage of filtering is accomplished by the dipole bending elements of the first section of the separator. The magnetic rigidity of the particles (in Tm) is related to their velocities and mass-to-charge ratio (A/Q) according to the following relativistic relation:

$$B\rho = 3.107\beta\gamma\frac{A}{Q} \qquad (1)$$

where $\beta = v/c$ and $\gamma = 1/\sqrt{1 - \beta^2}$ are the velocity and relativistic γ parameter, respectively. Since fragments produced by projectile fragmentation in a thick production target typically have very wide momentum distributions centered around the beam momentum [2], many of them fulfill the $B\rho$ condition and are transmitted through the momentum slits. For fully stripped ions ($Z = Q$), this is equivalent to a A/Z selection. As an example, Fig. 2 shows an identification plot after magnetic-rigidity filtering in the production of the nucleus ^{32}Mg by fragmentation of an ^{40}Ar primary beam on a 1.6 mm thick Be target. Many contaminants are present and the number of ^{32}Mg nuclei only amounts to 0.06% of the total intensity of the RNB. The optics of this first stage are usually set for a momentum-dispersive focus on the wedge absorber and momentum selection slits (see Fig. 1). Some fragment separators have more than one momentum dispersive plane, allowing one to place the momentum slits and wedge at different locations [3].
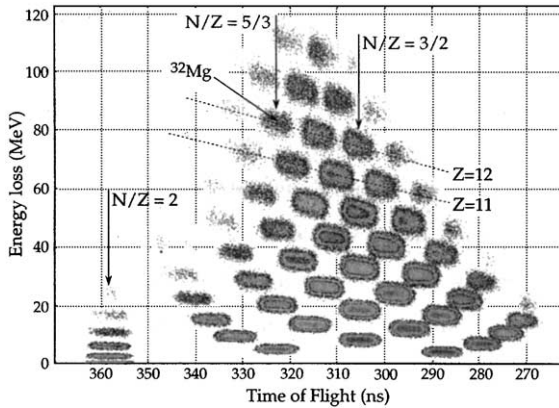
Fig. 2. Plot of transmitted fragments after magnetic rigidity filtering. The axes are energy loss (ordinate) and time-of-flight (abcissa). Each fragment is labeled and the intensity is color coded. The location of ^{32}Mg is indicated, as well as constant time-of-flight vertical lines corresponding to nuclei with same neutron-to-proton numbers N/Z. These lines arise from the magnetic rigidity filtering which transmits nuclei with the same mass-to-charge ratio A/Q at equal velocities (see Eq. (1)). This plot and subsequent identification plots are produced by a Monte-Carlo generator that mimics the experimental spectra observed on-line. Note that the Monte Carlo correctly simulates the behavior of the energy loss which decreases as the velocity increases, causing the ellipsoids corresponding to each nucleus to tilt.

2.2. Energy-loss filtering

The second method of filtering is based on energy loss in an absorber. A material is inserted at the dispersive focal plane between the two sections of the fragment separator. Because each fragment, depending on its atomic number and velocity, loses a different amount of energy ($\Delta E \propto Z^2/E/A$), its image at the final focus is centered at a different location. Using a set of slits after the second section, one can then select which fragments are transmitted. This method has been described elsewhere [1,3–5] and requires that the material be shaped as a wedge (or bent along a calculated curve for thin foils) in order to preserve the achromaticity of the separator. This can be understood qualitatively since for a given fragment different positions in the dispersive focal plane correspond to different velocities, and the energy loss must be adjusted accordingly by varying the
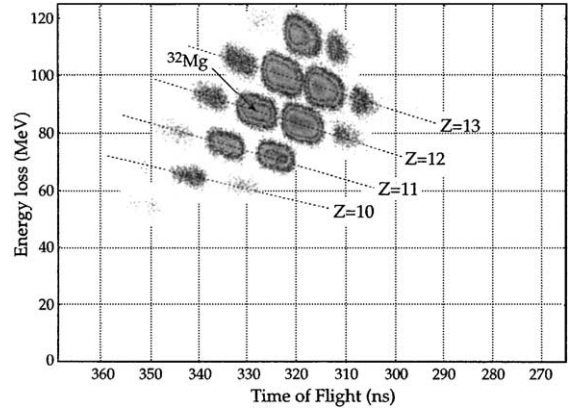

Fig. 3. Same as Fig. 2 but after energy-loss filtering. The wedge consists of a 500 μm thick beryllium foil bent to a shape calculated to preserve the achromatic focussing of the separator. The location of ^{32}Mg has slightly shifted to greater energy loss and longer time-of-flight because of the slowing down due to the insertion of the wedge. The number of contaminants is greatly reduced due to the additional $A^{2.5}/Z^{1.5}$ selection (see text).

thickness. In the program LISE, this method is referred to as "Wedge selection." Following our example from the previous section, Fig. 3 shows the same plot as Fig. 2 obtained after energy-loss filtering. The number of contaminants has been greatly reduced, and the number of ^{32}Mg nuclei now amounts to 20% of the total intensity. The transmitted fragments roughly follow a $A^{2.5}/Z^{1.5}$ dependence [4]. The combined first and second sections of the fragment separator are set as an imaging system with the transverse horizontal and vertical magnifications usually close to unity. However, to minimize the effects of straggling in the wedge, the magnification of the first section in the dispersive plane can be set to a value greater than 1, so that the second section can then be set to a magnification smaller than 1, hence reducing the spatial broadening of the image caused by the straggling in the wedge.

It should be noted that the level of purification achieved by the wedge selection depends on the following:

- the size of the primary beam spot on the production target;

- the magnification of the fragment separator;
- the thickness of the wedge;
- the setting of the slits located at the final focus.

As the thickness of the wedge is increased, greater separation can be achieved, but only up to a point where the straggling becomes too important and mixes the images of the various nuclei at the final focus. Each of the parameters upon which the selection depends can be adjusted in order to properly calculate the level of purification, and hence determine the optimum wedge thickness. The example shown in Fig. 3 only serves as an illustration and does not represent the optimum configuration for selecting ^{32}Mg.

In some other applications, it is desirable that the shape of the wedge inserted in the beam preserves another parameter of the beam, e.g. velocity. In that case, the wedge is called mono-chromatic and narrows the energy spread of the selected particles. This feature can be used in experiments where the nucleus of interest has to be stopped in a solid-state detector or a gas. The program gives four choices of wedge profiles: homogeneous, achromatic, monochromatic and custom. For wedges made of thin foils, the program also calculates the curve profiles for all choices.

2.3. Velocity filtering

Some experiments require a greater purity that can be achieved with energy-loss filtering. Some fragment separators have therefore added a third selection criterion based on velocity filters (Wien filters) [6]. These devices produce electric and magnetic fields perpendicular to each other. The momentum dispersion caused by the Wien filters can be compensated for by a small dipole placed downstream. The net result is a selection in mass of the remaining fragments. Fig. 4 shows the resulting identification plot, where the desired fragment, ^{32}Mg, is present at a 54% level of purity. Further purification would be possible by limiting the acceptances, but only at the expense of intensity.
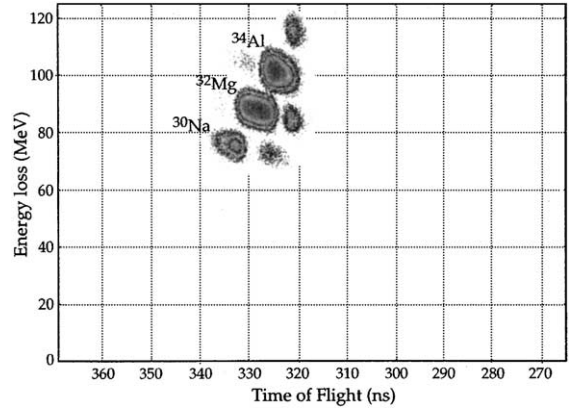

Fig. 4. Same as Figs. 2 and 3 but after velocity filtering.

3. Principle of calculations

The complete calculation of yields obtained in a fragment separator using projectile fragmentation involves different domains of physics. For a given ion, the yield can be written as the product of four independent factors

$$\mathcal{Y} = \mathcal{I}\mathcal{N}\mathcal{F}\mathcal{A} \tag{2}$$

where $\mathcal{I}$ is the primary beam intensity, $\mathcal{N}$ the probability of producing the nucleus of interest in the target, $\mathcal{F}$ the fraction of charge Q for the given charge state and $\mathcal{A}$ the total acceptance of the fragment separator. If the first factor ($\mathcal{I}$) is straightforward to calculate, the three others involve nuclear reactions, atomic interactions at high velocities, and ion optics calculations. In the following subsections we present the models used in LISE to calculate these three factors. As the program was intended to be a tool used during experiments, a major emphasis was placed on the speed of the calculations, avoiding lengthy calculations such as Monte-Carlo tracking simulations.

3.1. Target yield

The factor $\mathcal{N}$ in Eq. (2) represents the probability of producing the fragment of interest in the target. First we calculate the normalized total number of reactions $N_P(x)$ produced by a projectile P in a target slice ∂x at location x. This number

is governed by the following differential equation:

$$\frac{\partial N_P(x)}{\partial x} = [1 - N_P(x)]\sigma_P \tag{3}$$

where σ_P is the total reaction cross-section of the projectile. With the initial condition $N_P(0) = 0$, the solution to this equation is clearly

$$N_P(x) = 1 - e^{-x\sigma_P}. \tag{4}$$

Therefore, the number of incident projectiles available at thickness x to produce the nucleus of interest F is $1 - N_P(x) = e^{-x\sigma_P}$, and $\sigma_{P \to F}$ being the cross-section for producing the fragment F from projectile P, the number $N_F(x)$ of fragments F produced at thickness x follows the equation:

$$\frac{\partial N_F(x)}{\partial x} = [1 - N_P(x)]\sigma_{P \to F} = e^{-x\sigma_P}\sigma_{P \to F}. \tag{5}$$

The solution to this equation is

$$N_F(x) = \frac{(1 - e^{-x\sigma_P})\sigma_{P \to F}}{\sigma_P} \tag{6}$$

which in the case of a thin target can be approximated by

$$N_F(x) \approx \frac{[1 - (1 - x\sigma_P)]\sigma_{P \to F}}{\sigma_P} = x\sigma_{P \to F}. \tag{7}$$

Eq. (7) is the approximation used by default in the program LISE to calculate the target yield, in which it is simply proportional to the target thickness and the cross-section $\sigma_{P \to F}$. However, it becomes inaccurate when considering thicker targets and the production of very neutron-rich nuclei, as we shall see in the following.

3.1.1. One-step fragmentation

As the target thickness is increased, the probability of destroying the fragment of interest just produced by projectile fragmentation becomes significant. That probability is governed by the total reaction cross-section of the fragment σ_F. Taking this into account in Eq. (5) leads to the following differential equation:

$$\frac{\partial N_F(x)}{\partial x} = e^{-x\sigma_P}\sigma_{P \to F} - N_F(x)\sigma_F \tag{8}$$

the solution to which is

$$N_F(x) = \frac{e^{-x\sigma_F}[1 - e^{x(\sigma_F - \sigma_P)}]\sigma_{P \to F}}{(\sigma_P - \sigma_F)}. \tag{9}$$

The term $e^{-x\sigma_F}$ in Eq. (9) indicates that the number of fragments produced in the target will eventually decrease as the thickness is increased, as the probability of a second reaction destroying the previously made fragment also increases. However, this argument can be turned around: if the probability of having two successive fragmentations in the same target becomes non-negligible, then many other paths to produce the final fragment of interest can open.

3.1.2. Two-step fragmentation

In this process, the projectile undergoes a first fragmentation to produce an intermediate fragment i which in turn is fragmented to produce the final fragment of interest F. We already know from the previous section the number $N1_i(x)$ of intermediate fragments available to make a second fragmentation at thickness x (see Eq. (9)). The two-step fragmentation differential equation for the path going through intermediate fragment i is therefore

$$\frac{\partial N2_{i,F}(x)}{\partial x} = N1_i(x)\sigma_{i \to F} - N2_{i,F}(x)\sigma_F$$
$$= \left\{\frac{e^{-x\sigma_i}[1 - e^{x(\sigma_i - \sigma_P)}]\sigma_{P \to i}}{(\sigma_P - \sigma_i)}\right\}\sigma_{i \to F} - N2_{i,F}(x)\sigma_F \tag{10}$$

where σ_i is the total reaction cross-section of fragment i, and $\sigma_{P \to i}$ and $\sigma_{i \to F}$ are the cross-sections to produce i from P and F from i, respectively. The solution to this differential equation is

$$N2_{i,F}(x) = \{e^{-x\sigma_F}[e^{x(\sigma_F - \sigma_P)}(\sigma_F - \sigma_i)$$
$$+ e^{x(\sigma_F - \sigma_i)}(\sigma_P - \sigma_F)$$
$$+ \sigma_i - \sigma_P]\sigma_{P \to i}\sigma_{i \to F}\}/$$
$$\times [(\sigma_F - \sigma_i)(\sigma_F - \sigma_P)(\sigma_i - \sigma_P)] \tag{11}$$

and the total two-step fragmentation yield is the sum of all possible paths to produce the final fragment F:

$$N2_F = \sum_i N2_{i,F} = \sum_{Z_i = Z_F}^{Z_P} \sum_{N_i = N_F}^{N_P} N2_{i,F} \tag{12}$$

where $Z_{P,F}$, $N_{P,F}$ are the proton and neutron numbers of the nuclei involved in the reactions.
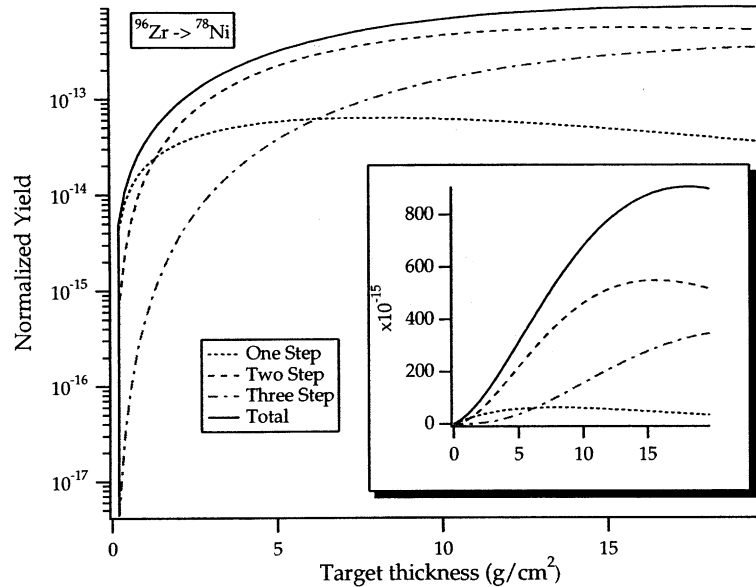
Fig. 5. Calculated target yields as a function of target thickness for the production of ^{78}Ni from a beam of ^{96}Zr on a Be target. The inset shows the same results plotted on a linear scale for a better view of the saturation effects. The cross-sections for producing the various fragments are calculated using the EPAX parametrization (see Section 3.2), and the total cross-sections using a simple geometric model. For thicknesses greater than 2 g/cm^2 the yield is dominated by multi-step processes. This dominance increases as the final fragment is chosen closer to the neutron drip-line.

Fig. 5 shows the evolution of the one-, two- and three-step fragmentation yields as a function of target thickness for the production of ^{78}Ni from a ^{96}Zr beam (the calculation of the three-step yield is given in the appendix). The inset shows the same data on a linear scale. Two- and three-step fragmentation become the dominant processes as the target thickness increases. Moreover, the saturation effect for the one-step yield occurs at a much smaller target thickness than for the two- and three-step yields. This implies that, regardless of all other parameters, the total yield can be increased more in a thicker target than when considering only one-step fragmentation. This effect is especially important when trying to reach the neutron drip-line, for which it is essential to limit neutron evaporation as much as possible. It is qualitatively easy to understand since the more nucleons are removed in a fragmentation, the more excitation energy the projectile-like fragment will have, and the more neutrons it will evaporate. As the cross-sections reflect this behavior, remov-ing fewer nucleons at a time in more than one fragmentation becomes more and more favorable towards the neutron drip-line. Fig. 6 illustrates this point for the two-step process in the case previously shown, the production of ^{78}Ni from ^{96}Zr. The figure shows a (N, Z) map of all possible intermediate fragments between the projectile and the final fragment. The size of each square represents the yield contribution of each intermediate fragment. Clearly the fragments located roughly along the straight line between the projectile and the final fragment are those which contribute the most, with an accentuated effect for the fragments with a neutron number closer to that of ^{78}Ni. As the target thickness increases, the two "cold fragmentations" going through those intermediate fragments quickly outweigh the one-step process for which 12 protons need to be removed in a single reaction.

To expedite the evaluation of the analytical formulas developed above, and in order to include all multi-step processes, the program LISE uses
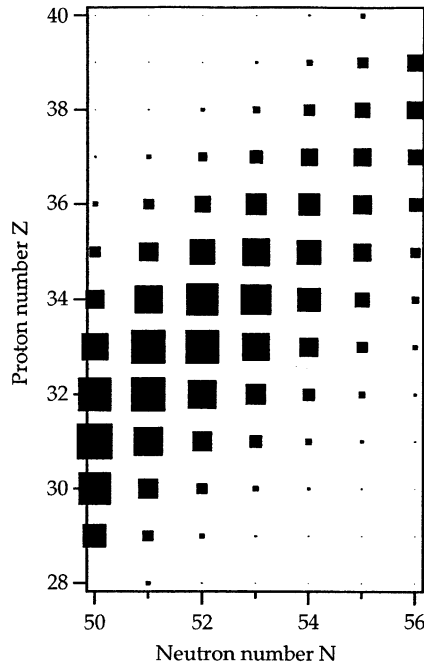
Fig. 6. Contribution yields from all possible intermediate fragments in a two-step fragmentation calculation for producing ^{78}Ni from a beam of ^{96}Zr. The size of the squares is proportional to the yield contributions. The domain in which the important contributions are found has a rhomboidal shape extending from the projectile to the fragment.

numerical integration. At each target slice dx, the yield of each fragment i produced by secondary reactions (i.e. other than the direct–one-step–fragmentation) is calculated using the formula

$$\mathrm{d}N_i = \sum_{j}^{\text{rhombus}} \sigma_{j\to i} N_j\,\mathrm{d}x - \sigma_i N_i\,\mathrm{d}x \qquad (13)$$

with initial conditions $N_i = 0$ and $N_P = 1$, where P stands for the projectile and i for the fragments. The summation in Eq. (13) is limited to a rhombus domain which includes the projectile and the fragment, in order to exclude contributions from negligible secondary reactions, as illustrated in Fig. 6. The contribution from secondary reactions is then added to the total yield of each fragment before the next iteration. The number of iterations can be varied and has a default value of 128.

3.2. Cross-sections

In the simplest description of a fragmentation reaction, the composition of the fragments is determined by the distribution of protons and neutrons at the instant of the reaction. This implies that the maximum cross-section is found for fragments having the same A/Z ratio as the projectile, and that the distributions are energy independent above a certain total kinetic energy of the projectile (the "limiting fragmentation" effect [7]). Indeed, it is clear from many experiments that neutron-rich projectiles produce neutron-rich fragments, and vice versa. However, because the excitation energy of the fragments is released mostly via particle emission, neutron evaporation is favored due to the Coulomb barrier. This effect tends to shift the cross-sections towards the proton drip line. For heavy projectiles such as ^{238}U, the energy release can lead to binary fission, which favors the production of fragments closer to the neutron drip-line [8]. At intermediate energies (10–100 MeV/u), it has been shown [9,10] that the projectile–target interaction time is long enough to equilibrate the A/Z ratio of the whole system (the "memory effect"). This has led to the use of neutron-rich or neutron-deficient targets to enhance the cross-section towards the drip-lines. At high energies, the use of very thick targets can lead to multi-step processes as we have seen in the previous section. Also, at energies up to a few GeV/u, Coulomb-induced fission of heavy projectiles can be used to produce neutron-rich nuclei [8], although this type of reaction should not be considered fragmentation.

The vast number of processes leading to the production of fragments makes it impossible to establish a single way of calculating the cross-sections based on the reaction processes. Rather, an empirical approach based on experimental results seems more appropriate. This is the basis of the EPAX [11,12] parametrization used in LISE. This parametrization is based on projectile and target fragmentation data and qualitatively reproduces predictions of intranuclear cascade calculations based on the Yariv–Fraenkel model [13]. Also, the parametrization reproduces around 85% of the 700 experimental fragmentation cross-

sections it is based on within a factor of 2. As a general rule, the parametrization is more likely to fail at greater distances from the valley of stability, where experimental cross-sections are unknown, and a small error in the exponential slope of the cross-section trend translates into a big error on the drip-line. Furthermore, it does not reproduce an effect clearly seen in experimental cross-sections, the additional binding due to the pairing of nucleons. This odd–even staggering becomes prominent at the drip-lines where only nuclei with an even number of drip-line nucleons remain bound. Consequently, the predictions of the EPAX parametrization have to be used with caution, especially on or near the drip-lines, and it is not unusual to observe differences of a factor of 5 or more with experiments. The program LISE offers the option of entering an experimentally known or better calculated cross-section for any given fragment, or selecting previous versions of the EPAX parametrization.

As this parametrization is based on experimental data, it likely already contains contributions from the multi-step secondary fragmentation processes. However, it is very difficult to infer the amount of these contributions since the parametrization is based on data coming from numerous sources. Their effect would be a scale down of the overall yield, but would not affect the qualitative conclusions given in the previous section. A more tangible approach would be to use a model such as the abrasion–ablation model to calculate the cross-sections used in the calculation of secondary reactions, to avoid the interference caused by the data and take into account binding energies in a more realistic way. A first attempt aimed at the study of the production of very neutron-rich nuclei using this model is under way [14].

Reactions where the final fragment has more neutrons or protons than the projectile are not covered by the EPAX parametrization. These reactions are referred to as transfer reactions, and are often used to produce radioactive beams close to the valley of stability with very high intensities. The program LISE uses and extrapolation of the EPAX parametrization to calculate the cross-sections, but they should be taken with extreme caution since the actual cross-sections clearly depend on the details of the reactions as well as the beam energy.

3.3. Fragmentation

In order to calculate the acceptance factor $\mathscr{A}$ in Eq. (2), it is necessary to evaluate the phase-space distributions of the fragments produced in the target. A simple picture of the projectile fragmentation process used to produce RNBs is a peripheral collision resulting in a sudden ablation of part of the projectile by the target [15]. The number of nucleons removed depends on the impact parameter and the emerging fragment is composed of the so-called "spectator" nucleons. It has an intrinsic excitation energy due to its deformation and the abrasion process. The fragments then undergo deexcitation by particle emission and/or γ-ray cascade. Their intrinsic momenta are determined by the contributions of each nucleon's momentum at the instant of the reaction. The fragmentation process has been studied extensively [16] and many papers have describe models that predict the characteristics of the fragments. For the program LISE, the most important factors are the momentum width and energy damping produced by the reaction. The momentum width directly affects the number of fragments collected in the acceptance of the fragment separator, while energy damping lowers the energy—and therefore the magnetic rigidity $(B\rho)$—of any given fragment.

In an early paper [17], Goldhaber proposed a simple formula for the momentum width of fragments produced by high-energy projectile fragmentation

$$\sigma^2 = \sigma_0^2 \frac{A_F(A_P - A_F)}{A_P - 1} \tag{14}$$

where A_F and A_P are the fragment and projectiles masses, respectively, and σ_0 is related to the Fermi motion of the nucleons inside the projectile according to $\sigma_0^2 = \frac{1}{5}P_F^2$. In the relativistic energy regime, the transverse and longitudinal momentum widths of the fragments are similar. However, studies in the intermediate energy domain (10–100 MeV/u) [18,19] show that the transverse momentum width of the projectile-like fragments

is by far greater than the longitudinal. Part of this difference can be attributed to Coulomb and nuclear deflection of the fragment by the target residue and ejected protons during the fragmentation. The following formula has been proposed to describe the perpendicular width [19]:

$$\sigma_\perp^2 = \sigma_0^2 \frac{A_F(A_P - A_F)}{A_P - 1} + \sigma_D^2 \frac{A_F(A_F - 1)}{A_P(A_P - 1)} \quad (15)$$

where σ_D is called the orbital dispersion, and has a typical value of 200 MeV/c. Whereas this formula is able to reproduce the data from Ref. [19] at 100 MeV/u, it fails to do so at 44 MeV/u [18]. This discrepancy can be attributed to the additional energy damping observed at 44 MeV/u, which is also responsible for the low-energy tails observed in the distributions.

In the program LISE, the parallel momentum width $\sigma_\parallel$ can be calculated according to four different parametrizations. They are successively formula 14 from Ref. [17], a similar parametrization found in Ref. [20], the fragmentation model of Friedman [21], and finally our own parametrization [22] which uses a convolution of a Gaussian with an exponential tail at low energy. This last parametrization reproduces well the data observed at intermediate energy (10–100 MeV/u), where dissipative effects still play an important role. The shape and width of the parallel momentum distribution directly affect the transmission through the momentum acceptance.

For the transverse momentum width $\sigma_\perp$, which affects the transmission through the solid angle acceptance, formula 15 is used. The values of σ_0 and σ_D can be adjusted, from default values of 90 and 200 MeV/c, respectively.

The ratio of the fragment mean velocity to the beam velocity is determined by the energy damping of the reaction. Four different choices for calculating this ratio are also possible: it can either be held at a fixed value, or calculated using one of the three parametrizations of Refs. [23,24] or Ref. [22]. Some of the parameters used in these parametrizations can be modified, for instance in the parametrization of Ref. [23], the amount of energy necessary to remove each nucleon from the projectile, which has a default value of 8 MeV.

3.4. Phase-space distributions

To calculate the selections and transmissions of a fragment separator, the phase-space distributions corresponding to a given fragment have to be propagated through its different sections. Furthermore, selection and acceptance cuts are usually performed by means of slits which are located at various image points along the device. This requires the possibility of propagating phase-space distributions from one image to another, taking into account the effects of previous cuts. Because of these constraints, phase-space distributions can have arbitrary shapes; simplifications such as Gaussian line shapes are not valid. A typical example is the momentum distribution of a fragment produced in a thick target, the usual case in a fragment separator. Whereas the distribution from projectile fragmentation is well approximated by a Gaussian, the distribution which originates from the energy loss in the target on the other hand, is a Heaviside or square distribution. The convolution of the two produces a "rounded edge" square-like momentum distribution which is difficult to model.

A standard method used to propagate such distributions is Monte-Carlo tracking where the initial coordinates of the particles are sampled according to the calculated phase-space distribution, and then propagated through each element of the system [25]. For our purpose however, this method is not practical because of the computation time required for each fragment, since the sampling has to cover the six-dimensional phase space. To remedy to this problem, we have developed a new method to quickly compute the time evolution of arbitrary phase-space distributions. The details of the method are published elsewhere [26]. It is based on the reduction of a transport integral which has the form

$$D'(q_1', ..., q_n') = \int_1 \cdots \int_n dq_1', ..., dq_n' D(q_1, ..., q_n)$$
$$\times \prod_{i=1}^n \delta(q_i' - f_i(q_1, ..., q_n)) \quad (16)$$

where D is the initial phase-space distribution at time t and D' is the resulting phase-space

distribution at time t'. The $q_1, \ldots, q_n$ and $q'_1, \ldots, q'_n$ represent the phase-space coordinates at t and t', respectively. The core of this integral is the set of functions $f_i(q_1, \ldots, q_n)$, which describe how each of the final coordinates depends on the initial ones. The Dirac δ function merely selects the combinations of initial coordinates which give a contribution at the final coordinate q'_i. In practical calculations one is more interested in the projections of the final phase-space distributions which can be reduced to

$$P'_i(q'_i) = \int_1 \cdots \int_n D(q_1, \ldots, q_n)$$
$$\times \delta(q'_i - f_i(q_1, \ldots, q_n)) \, dq_1, \ldots, dq_n \qquad (17)$$

which can be understood as the weighted sum of the points of the distribution $D(q_1, \ldots, q_n)$ which are mapped into q'_i by the function $f_i(q_1, \ldots, q_n)$. Under the assumptions of an incoherent object and first-order approximation, this integral can be reduced to convolution products of the form [26]

$$P'_i(q'_i) = \frac{1}{\prod_{k=1}^n R_{ik}} [\bar{P}_1 \otimes \bar{P}_2 \otimes \cdots \otimes \bar{P}_n] (q'_i) \qquad (18)$$

where R_{ik} are the first-order coefficients which describe the transport function $f_i(q_1, \ldots, q_n) = \sum_{k=1}^n R_{ik} q_k$, and $\bar{P}_k(p_k) = P_k(p_k/R_{ik}) = P_k(q_k)$ with the variable change $p_k = R_{ik} q_k$. The convolution products are computed using fast-Fourier transform techniques.

In beam optics, the phase space is usually defined in terms of the variables $(x, \theta, y, \phi, l, dp)$ where (x, θ) and (y, ϕ) are the positions and angles in the dispersive and non-dispersive planes, respectively. The program LISE assumes the structure shown in Fig. 1 for the fragment separator, with a focalized incoherent object at the target, dispersive focus at the intermediate image, and an achromatic final image, meaning that the position and angle in the dispersive plane do not depend on the momentum. However, the last version (4.11) allows non-zero $(x|\theta)$ and $(y|\phi)$ terms in the matrix, meaning that focussing is no longer assumed by default. First-order coefficients calculated with a beam optics program such as TRANSPORT [27] are entered in the program and can be altered interactively. This provides the possibility of simulating different devices or different optical modes of a given device.

3.5. Energy loss and stragglings

The calculation of energy loss in materials is most efficiently performed using a backward interpolation using a table of range calculations. The kinetic energy left after passing through a thickness Δx of material is equal to $E_i - \Delta E$ where E_i is the initial energy and ΔE the energy loss. If $R(E)$ is a function giving the range at a given energy E, then in terms of range one can write

$$R(E_i) = \Delta x + R(E_i - \Delta E). \qquad (19)$$

The energy loss ΔE can be calculated from a range table of the particular particle into the particular material by first interpolating in energy to get $R(E_i)$, and then in range to get $E_i - \Delta E$ and hence the energy loss. This method is much faster than the direct integration of the energy loss using $\Delta E = \int_{\Delta x} \partial E/\partial x \, dE$ with the same accuracy. Because it is impractical to pre-calculate range tables for all combinations of particles and materials, the program LISE calculates the required tables on the fly and stores them as they occur. The range calculations are based either on the formulas of Hubert et al. [28,29] for heavy ions of energies from 2.5 MeV/u to 2 GeV/u in solids, or the hydrogen-based stopping power formulas of Ziegler et al. [30], depending on the user's choice. For very low-energy particles (down to 10 keV/u), nuclear stopping corrections are added. The program calculates energy losses in gaseous materials, as well as composite materials. A list of many common composites is available in a menu, but any combination of up to five different elements can be composed.

The energy straggling is calculated (in MeV) from a semi-empirical formula [31] based on Bohr's classical formula

$$\delta(\Delta E) = k Z_P \sqrt{Z_T t / A_T} \qquad (20)$$

where Z_P is the atomic number of the projectile, Z_T and A_T the atomic and mass numbers of the material and t the thickness in g/cm^2. The parameter k increases logarithmically with incident energy, and is parametrized from experimental

data. Its value ranges approximately from 1 (at 1 MeV/u) to 2.5 (at 1 GeV/u).

The multiple angular straggling is determined using the formula derived in Ref. [32] where the "reduced angle" $\tilde{\alpha}_{1/2}$ follows a simple power law fitted to the experimental data

$$\tilde{\alpha}_{1/2} = 1.00\tau^{0.55} \tag{21}$$

where τ is the "reduced thickness" given by $\tau = \pi a^2 N t$. Here the screening parameter $a = 0.885 a_0 / \sqrt{Z_P^{2/3} + Z_T^{2/3}}$ where $a_0 = 0.529 \times 10^{-8}$ cm, Z_P and Z_T are the atomic numbers of the projectile and material, N the number of scattering centers per unit volume and t the penetrated thickness. The scattering angle $\alpha_{1/2}$ is then deduced (in mrad) from the expression for the "reduced angle": $\tilde{\alpha}_{1/2} = \alpha_{1/2} E a / 2 Z_P Z_T e^2$, where E is the energy of the projectile and e the electronic charge.

3.6. Charge states

Charge-state distributions are important in the determination of yields as the magnetic rigidity filtering stage of the separator is sensitive to the charge of the particles (see Section 2.1). Ab initio calculations are difficult because they require knowledge of a huge number of cross-sections and their variations as a function of energy. Better results are obtained using semi-empirical formulae fit to a set of data points. They provide a determination of the mean charge state as well as the width of the distribution. The early version of LISE used a parametrization from Ref. [33]. More recently, an extensive set of measurements has been used to determine a more accurate parametrization [34]. At low energy (up to 6 MeV/u), the parametrization from Ref. [35] can be used. All three are available in the program.

A particularly important advantage of calculating charge-state distributions becomes apparent when fragmenting heavy beams (typically those between krypton and uranium at energies $E < 100$ MeV/u), for which each fragment may be produced in various charge states, rather than fully stripped. In that case, the identification plots usually used become much more difficult to interpret without the help of a calculation. For instance, a regular time-of-flight vs energy-loss spectrum will show charge states of different nuclei superimposed (see Section 5.1). A precise, independent measurement of the kinetic energy of the fragments, e.g. with solid-state detectors, is necessary in order to sort out the different charge states. LISE can calculate the energy losses and ranges of the transmitted fragments in various materials, and hence simulate any particular detector setup. Then identification plots using these calculations can be produced and directly compared to on-line data during an experiment.

Another important feature of the charge-state distributions is the ability to calculate their evolution as the ions traverse materials of different compositions and thicknesses. For instance, stripping foils of low atomic number (Z) are often used as a backing of high-Z production targets. This has the effect of shifting the charge-state distributions towards fully stripped ions in order to increase the yield of the most intense charge state. Likewise, the use of a wedge absorber in the energy-loss filtering method can modify the charge-state distributions and affect the optimum setting of the second section of the fragment separator. For these reasons, the program LISE calculates the charge-state distributions after every material inserted in the path of the beam.

4. Description of the computer program

The program is constantly being improved, guided by the feedback of the users. At the time of this writing, the current version is 4.11, which is described in this article. This paper is not an exhaustive description of LISE and its many features. The reader is invited to obtain the program and study the extensive manual, or better yet, install it and practice using it directly. An on-line help feature is available in the program which provides information on most of its features.

4.1. User interface

Fig. 7 shows an example of the main window of the program. Most of the display is occupied by
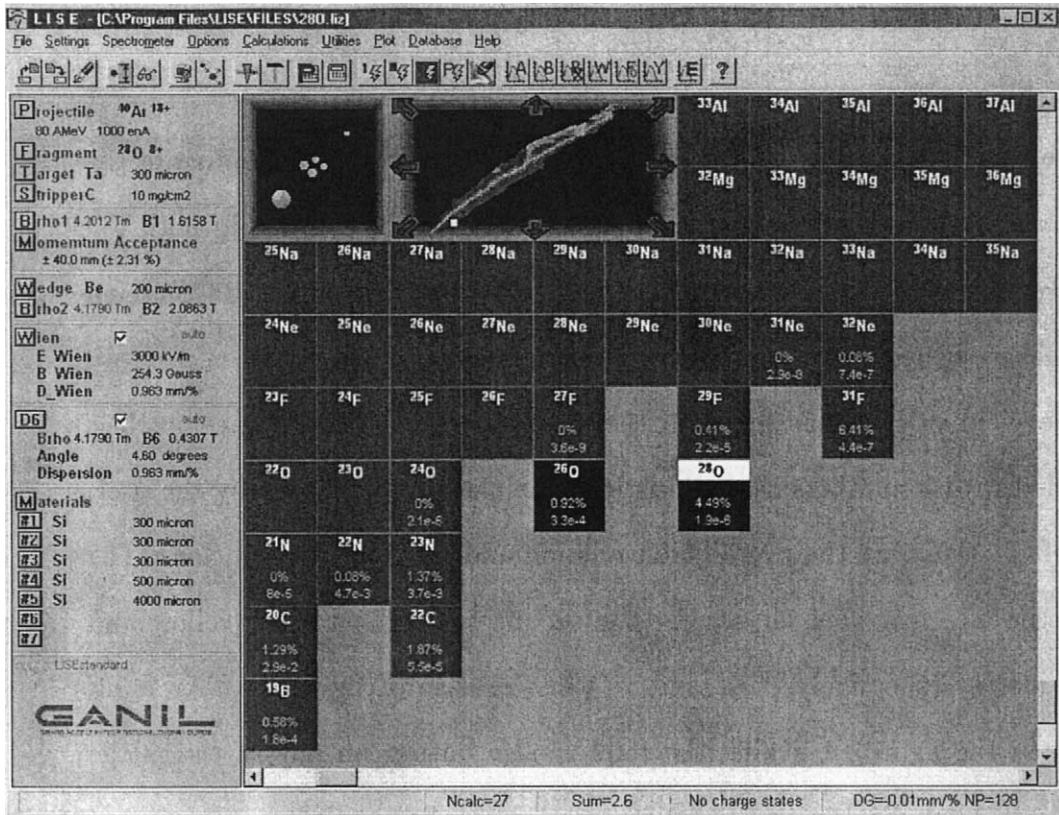
Fig. 7. Example of the main window of the program LISE (the actual window is displayed in color). The small map located on top provides shortcuts to all regions of the chart of nuclei. See the text for details.

the chart of nuclei, which can be scrolled in both the number of protons (vertical) or neutrons (horizontal). For convenience, an optional navigation map allows one to jump directly to the region of interest. As the yield calculations proceed, the boxes corresponding to each nucleus are filled with two numbers characteristic of the calculation chosen by the user. By default these are the overall transmission and yield for each nucleus. The projectile and fragment chosen for the setting are indicated by yellow and white strips, respectively, ^{40}Ar and ^{28}O in the case of Fig. 7 (^{40}Ar is off screen in the figure). Clicking the right mouse button on any of the nuclei opens a window displaying all the information for that nucleus.

The area located on the right of the chart of nuclides contains panes which display the current settings of the fragment separator. Buttons located on each pane allow easy access to the corresponding parameters. Other buttons located on top are shortcuts to the most common tasks of the program, such as file opening and saving, etc. Placing the mouse over any of those buttons opens a small explanation box. Finally, the menu bar provides access to all the features of the program.

4.2. Configuration files

The program LISE can be used to calculate yields for any fragment separator very easily using configuration files. These files contain information required to perform the calculations, e.g. primary beam characteristics, acceptances and optics coefficients. All parameters can be interactively modified and later saved as a new configuration. The default configuration is for the GANIL fragment

separator LISE, and standard configuration files for several other fragment separators are distributed with the program.

4.3. Outputs and plots

In addition to a standard output file containing information about the current calculation, LISE
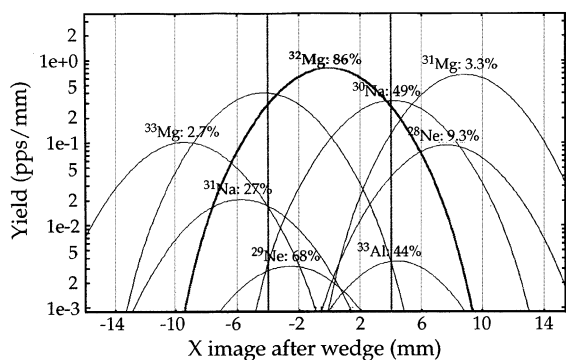

Fig. 8. Wedge selection plot showing the location of images corresponding to different nuclei at the achromatic focal plane. The slits are indicated as the two vertical lines.

can produce a number of plots showing different aspects of the phase-space distributions as they occur along the fragment separator. As an example, Fig. 8 shows the images of various nuclei calculated at the focal plane. The slits are represented by two vertical lines and the vertical axis is logarithmic as the yields differ by several orders of magnitude. The plot shows that among the fragments produced from the ^{40}Ar beam, only nuclei in the vicinity of ^{32}Mg are transmitted because their images end up at similar locations in the focal plane. As the number of protons and neutrons differs more and more from those of the chosen fragment, the images get shifted away from the slits and their transmissions (indicated in %) become smaller.

The full power of the Monte-Carlo generator presented in earlier identification plots becomes apparent when calculating energy losses and ranges in foils or detectors. Fig. 9 shows an example of an energy loss vs total energy plot for nuclei implanted in two silicon detectors of thicknesses 100 and 200 μm. The energy loss in the 100 μm detector shows the characteristic
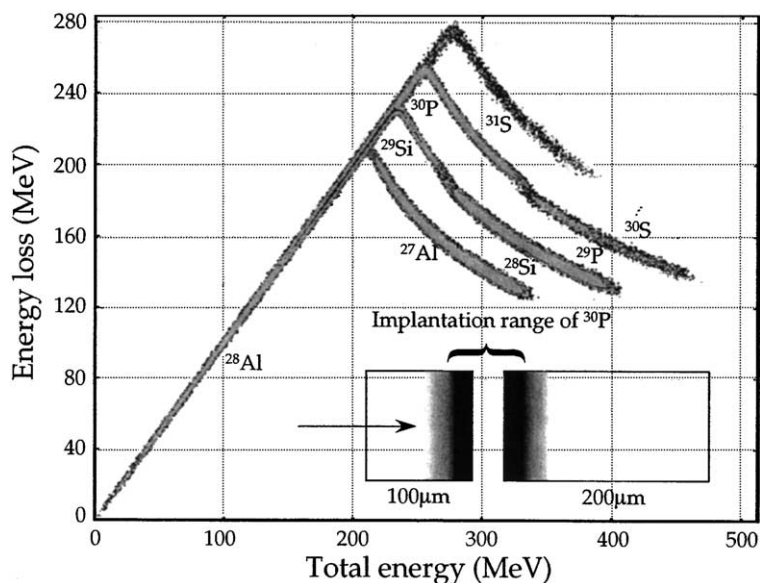

Fig. 9. Calculated energy loss vs total energy plot for a few nuclei produced in the fragmentation of ^{40}Ar at 50 MeV/u. Half of the desired fragments, ^{30}P, are implanted in the 100 μm detector, half in the following 200 μm detector. The contaminants are implanted at different locations due to their different masses, charges and energies. Some of them completely punch through the 100 μm detector (^{27}Al, ^{28}Si, ^{29}P and ^{30}S).

inflection point corresponding to the energy at which the nuclei are no longer implanted and punch through. Such a simulation is extremely useful in experiments where the implantation of a given nucleus has to be carefully adjusted. Note that no pulse-height defects are included in the energy loss calculations at present.

4.4. Extra features and utilities

In this section we concentrate on the most important features only, as other features are too numerous to be fully listed here.

4.4.1. Yield and transmission optimizations

One of the most important parameters the experimenter needs to determine prior to forecasting fragmentation yields is the target thickness. As the target thickness increases, the number of target nuclei interacting with the beam also increases, but so does the energy loss. In particular, the difference in energy loss between fragments produced from the front and the back of the target leads to a broadening of the momentum distribution which becomes rapidly much larger than most fragment separator momentum acceptances. As a result, the number of transmitted fragments decreases, and there is a thickness for which these two competing effects induce a maximum yield. This maximum depends on the initial parameters of the primary beam and target used, as well as on the fragment chosen for optimization. Other effects such as straggling also increase with target thickness and limit the transmission. An example of a target-thickness optimization calculated by LISE is shown in Fig. 10 for the case of ^{32}Mg produced from a primary beam of ^{40}Ar.

Once the optimum target thickness has been determined, the program can calculate the magnetic rigidity and velocity filter settings to transmit the desired fragment. If a wedge absorber is used or other materials (such as detectors) are inserted into the path of the beam, the program adjusts the settings accordingly. These calculations can also be performed in a reverse manner, in which the user specifies a desired energy or magnetic rigidity, and the program calculates the amount of material
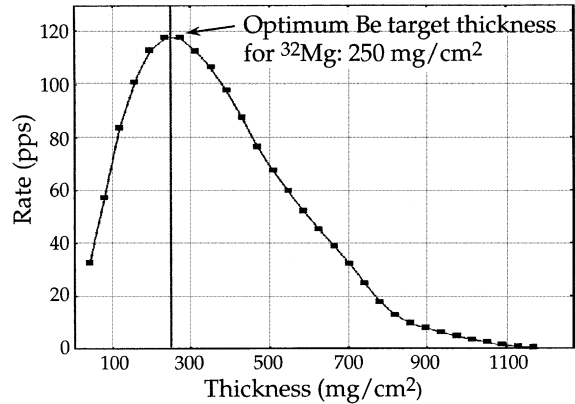

Fig. 10. Calculated target optimization plot. An optimal target thickness of 250 mg/cm^2 is found at the maximum of the distribution.

needed to reach it. This feature is especially useful in experiments where nuclei must be implanted at a specific depth in a foil or a detector.

After the parameters of the fragment separator have been set, the program can calculate the transmission of any nucleus, based on the optics as well as the positions of the various slits located along the beam line. Any modification of these parameters automatically clears the transmission data, which then must be recalculated.

4.4.2. Physical parameter calculator

It is often important to calculate various physical parameters such as energy, magnetic rigidity, energy loss, range, for a given ion. This is the purpose of the physical calculator with which the user can quickly determine energy losses, ranges and stragglings in any kind of material or composite at any location along the beam line. This feature is especially useful when planning implantation experiments where the nuclei of interest must be stopped in a medium for later study (e.g., radioactive decays, nuclear magnetic moments, etc.). The calculator also features "backward" energy loss and range calculations in which the initial energy necessary to obtain the desired final energy or range is calculated. The required amount of a given material to slow down particles from initial to final energies can also be determined. Fig. 11
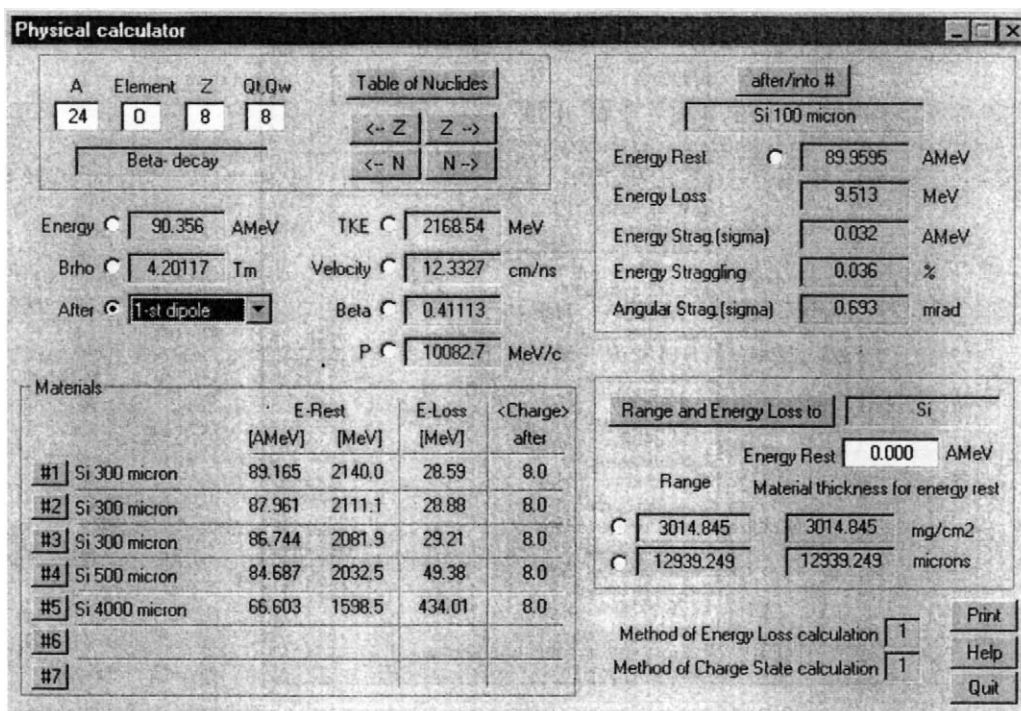
Fig. 11. Physical calculator window showing various calculations performed for the nucleus ^{24}O. The energy can be entered not only by the different parameters such as magnetic rigidity, velocity or momentum (radio buttons on the left), but also by specifying either an energy after a given material (top right) or the total range (bottom right).

shows the physical calculator window. Various radio buttons allow one to choose the method of calculation and which parameter is entered. The ion is selected on the top pane of the window, and calculations are performed in up to seven materials.

4.4.3. Reaction kinematics

Two-body reaction kinematics and Q-values can easily be calculated within the framework of LISE. Plots of the center-of-mass and laboratory scattering angles vs energy can be produced and saved to disk. The calculations are fully relativistic.

4.5. Database

The program LISE has a built-in database which contains basic information on nuclei. It is based on the 1995 Atomic Mass Evaluation [36,37] for known or estimated mass excesses and related

quantities, and other sources [38,39] for the half-lives. Plots of different quantities can easily be made as a function of atomic number Z, mass A, neutron number N or isospin N–Z. As for all monodimensional plots, the data can be saved to a file in ASCII format for use by an external program. Fig. 12 shows an example of the database entry window. The user can quickly navigate through the table of nuclei using the atomic number and neutron number arrows. The database information is also included in the statistics window activated by right clicking on any nucleus directly on the table of nuclei display.

4.6. On-line help

A fully featured on-line help facility is available, containing a table of contents as well as an index and search engine. The commands are explained in detail, both from the menu system and the toolbar.

Fig. 12. Database entry window. See text for details.

A history of changes made in various versions is also included which describes the new features added since the first Windows[TM] 98 version. Finally, a reference manual provides additional information on the principles of the calculations, as well as a tutorial to guide new users.

5. Comparison with data

As an example of the results and help provided by the program LISE during an experiment, we present a quantitative comparison with data obtained from the fragmentation of ^{86}Kr beams at 60 MeV/u on a composite Ni (100 µm) and Be (500 µm) target [40]. The particle identification in this experiment is complicated by the fact that the heaviest fragments emerge from the target with more than one charge state. Because the Bρ selection is sensitive to the charge of the ions, different mass and charge combinations of an isotopic line can get mixed on the regular energy-loss vs time-of-flight identification plot.

5.1. On-line identification

Fig. 13 shows a qualitative comparison between the LISE calculation and the data taken at Bρ = 2.367 Tm. The mixing of different masses and charge states is clearly visible for fragments between Cr and Ge. The lighter fragments appear to emerge fully stripped, and the $A/Z = 2$ vertical lines can be seen on the lower right corners of the spectra. To separate the different charge states, an additional measurement is necessary. Usually the total kinetic energy of the fragments can be measured by stopping them in silicon detectors. Then the charge state of each individual ion can be determined and used to gate the identification plot. Fig. 14 shows the same comparison between calculation and data for fully stripped ions only ($Z - Q = 0$). The masses of isotopes between Cr and Ge are now clearly resolved.
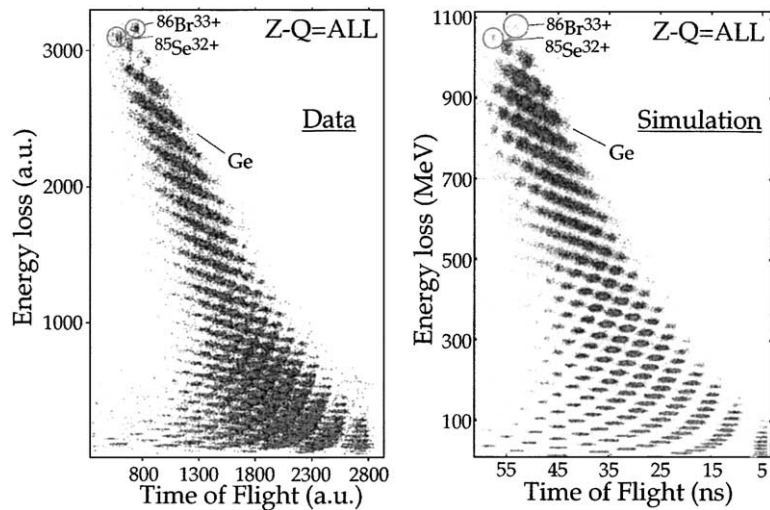
Fig. 13. Energy loss vs time-of-flight identification plots. The spectrum on the left contains the data taken during the experiment. The spectrum on the right is the LISE simulation. The isotopic lines between Cr and Ge clearly show different charge states and masses mixed together.
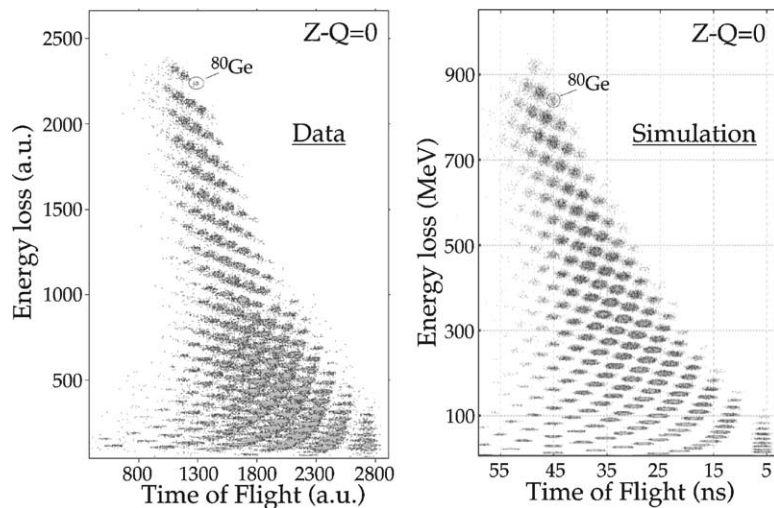

Fig. 14. Same as Fig. 13 but gated on the fully stripped ions. Now each mass can be clearly separated for the nuclei between Cr and Ge.

The real power of the simulation is more apparent when an energy-loss wedge is used to further select specific isotopes. As another example, we take the recent discovery of the doubly magic nucleus ^{48}Ni [41] for which a ^{58}Ni at 74.5 MeV/u projectile was used on a Ni target, followed by a Be wedge. Fig. 15 shows the comparison between the experimental and calculated energy loss vs time-of-flight spectra. Because only part of the usual "tree" pattern is visible, it is much more difficult to identify the group of events corresponding to a given nucleus. By comparing the data with the simulation though, this task becomes straightforward as the calculated pattern
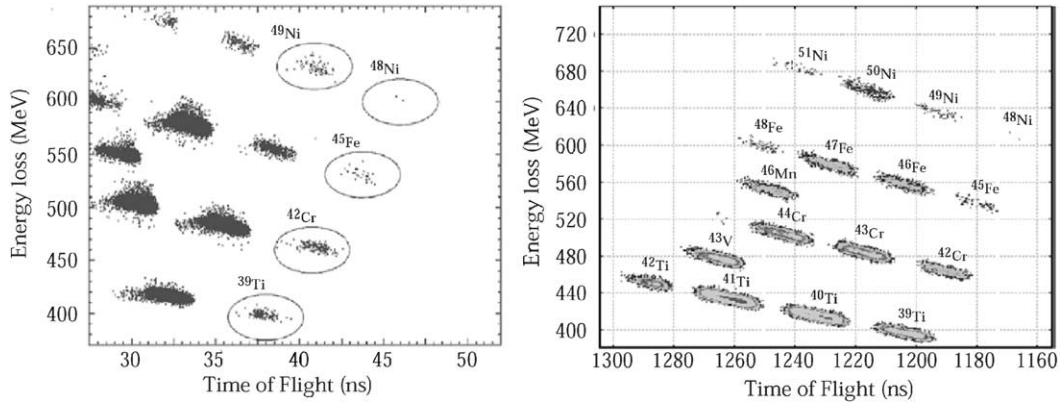
Fig. 15. Comparison between experimental and calculated identification plots. The spectrum on the left is taken from Ref. [41], and the spectrum on the right is the LISE simulation. The pattern observed in the experiment is readily recognized in the simulation, and makes the assignments straightforward.

closely matches the data. The simulation proves to be especially useful in such a low-yield experiment (less than one ^{48}Ni nucleus was produced per day [41]) where it is essential to be able to verify that the settings of the fragment separator are correct without actually seeing the whole spectrum, relying on the most copiously produced nuclei to check the identification.

Note that both the time-of-flight and the energy loss can be calculated absolutely, provided the flight path and detector thickness are known, and the experimental spectra are properly calibrated. In Fig. 15 the energy loss scale has been calibrated, which provided an additional check on the identification of the nuclei.

5.2. Yields

Fig. 16 shows a quantitative comparison between the observed and calculated yields in the fragmentation of a ^{86}Kr beam at 60 MeV/u. The isotopic distributions are plotted for elements from Ti to Ge, for fully stripped ions on the top and hydrogen-like ions on the bottom. Overall the agreement is quite good, except in the case of Cu and Ge isotopes for which the absolute magnitudes of the yields are underestimated and overestimated, respectively, by about a factor of 2 in the case of the fully stripped ions.

Note that contrary to the fully stripped ions, the yields of hydrogen-like ions decrease for smaller atomic numbers. This is due to the one-electron charge state cross-section which drops sharply as the Coulomb field of the nuclei decreases.

6. Conclusion

The program LISE described in this paper simulates the operation of dipole-based fragment separators used to produce radioactive beams via projectile fragmentation. It can be used not only to forecast the yields and purities of radioactive beams, but also as an on-line tool for beam identification and tuning during experiments. Its interface and algorithms are designed to provide a user-friendly environment allowing easy adjustments of the input parameters and quick calculations. It can be configured to simulate the fragment separators of various research institutes by means of configuration files. The program LISE is constantly updated and improved upon requests from the users. It is readily available on the World Wide Web and runs on PC (Personal Computer) platforms, as well as on Windows^{TM} 95 and 98 emulators on other platforms such as Unix or MacOS^{TM}.
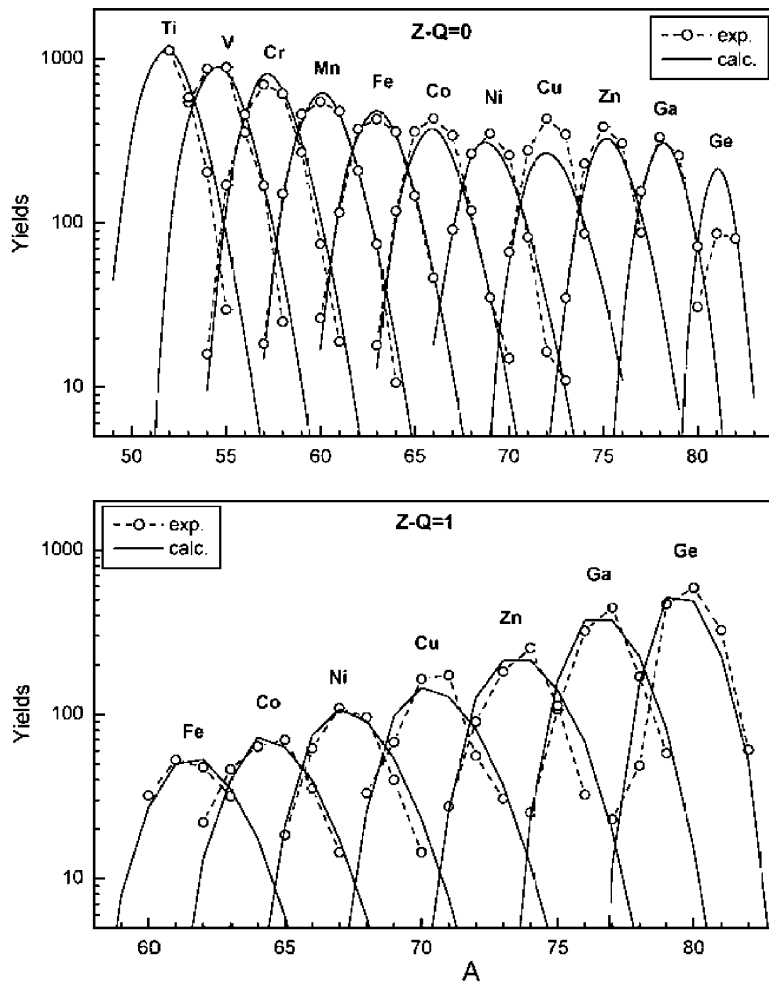
Fig. 16. Quantitative comparison between observed and calculated yields in the fragmentation of a ^{86}Kr beam at 60 MeV/u. The top figure shows the yields for fully stripped ions, and the bottom figure the yields for hydrogen-like ions.

Acknowledgements

Appendix

Three-step fragmentation yields are obtained in the same way as two-step fragmentation yields. Knowing the number of fragments produced via a two-step process from Eq. (11), the same type of differential equation can be written

$$\frac{\partial N3_{i,j,F}(x)}{\partial x} = N2_{i,j}(x)\sigma_{j \to F} - N3_{i,j,F}(x)\sigma_F$$
$$= \{e^{-x\sigma_j}[e^{x(\sigma_j - \sigma_P)}(\sigma_j - \sigma_i)$$
$$+ e^{x(\sigma_j - \sigma_i)}(\sigma_P - \sigma_j) + \sigma_i - \sigma_P]\sigma_{P \to i}\sigma_{i \to j}\}/$$
$$[(\sigma_j - \sigma_i)(\sigma_j - \sigma_P)(\sigma_i - \sigma_P)] * \sigma_{j \to F}$$
$$- N3_{i,j,F}(x)\sigma_F \qquad (A.1)$$

where $\sigma_{i \to j}$ and $\sigma_{j \to F}$ are the cross-sections for producing the intermediate fragment j from i and F from j, respectively. The solution to this

differential equation is

$$
\begin{aligned}
N3_{i,j,F}(x) = \{ & e^{-x\sigma_F}[(-1+e^{x(\sigma_F-\sigma_i)})\sigma_j(\sigma_j-\sigma_P)\sigma_P \\
& + \sigma_F^2[-e^{x(\sigma_F-\sigma_j)}\sigma_i+e^{x(\sigma_F-\sigma_P)}(\sigma_i-\sigma_j) \\
& + e^{x(\sigma_F-\sigma_i)}\sigma_j-e^{x(\sigma_F-\sigma_i)}\sigma_P+e^{x(\sigma_F-\sigma_j)}\sigma_P] \\
& + \sigma_i^2[(-1+e^{x(\sigma_F-\sigma_P)})\sigma_j-[-1+e^{x(\sigma_F-\sigma_j)}]\sigma_P] \\
& + \sigma_F[e^{x(\sigma_F-\sigma_j)}\sigma_i^2+e^{x(\sigma_F-\sigma_i)}\sigma_j^2 \\
& + e^{x(\sigma_F-\sigma_P)}(-\sigma_i^2+\sigma_j^2)+e^{x(\sigma_F-\sigma_i)}\sigma_P^2-e^{x(\sigma_F-\sigma_j)}\sigma_P^2] \\
& - \sigma_i[-(-1+e^{x(\sigma_F-\sigma_P)})\sigma_j^2 \\
& + [-1+e^{x(\sigma_F-\sigma_j)}]\sigma_P^2]]\sigma_{P\to i}\sigma_{i\to j}\sigma_{j\to F}\}/ \\
& \times [(\sigma_F-\sigma_i)(\sigma_F-\sigma_j)(\sigma_i-\sigma_j) \\
& \times (\sigma_F-\sigma_P)(\sigma_i-\sigma_P)(\sigma_j-\sigma_P)].
\end{aligned} \tag{A.2}
$$

The total three-step fragmentation yield is obtained by summing the individual yields over all possible paths to produce the final fragment

$$
\begin{aligned}
N3_F &= \sum_i \sum_{j<i} N3_{i,j,F} \\
&= \sum_{Z_i=Z_F}^{Z_P} \sum_{N_i=N_F}^{N_P} \sum_{Z_j=Z_F}^{Z_i} \sum_{N_j=N_F}^{N_i} N3_{i,j,F}.
\end{aligned} \tag{A.3}
$$

References

[1] R. Anne, et al., Nucl. Instr. and Meth. A 257 (1987) 215.
[2] G.D. Westfall, et al., Phys. Rev. Lett. 43 (1979) 1859.
[3] B.M. Sherrill, et al., Nucl. Instr. and Meth. B 56/57 (1991) 1106.
[4] J.P. Dufour, et al., Nucl. Instr. and Meth. A 248 (1986) 267.
[5] K.-H. Schmidt, et al., Nucl. Instr. and Meth. A 260 (1987) 287.
[6] R. Anne, A.C. Mueller, Nucl. Instr. and Meth. B 70 (1992) 276.
[7] E.M. Friedlander, H.H. Heckmann, in: D.A. Bromley (Ed.), Treatise on Heavy Ion Science, Vol. 1, Plenum, New York, 1985, p. 102.
[8] M. Bernas, et al., Phys. Lett. B 331 (1994) 19.
[9] D. Bazin, et al., Nucl. Phys. A 515 (1990) 349.
[10] O.B. Tarasov, et al., Nucl. Phys. A 629 (1998) 605.
[11] K. Sümmerer, et al., Phys. Rev. C 42 (1990) 2546.
[12] K. Sümmerer, B. Blank, Phys. Rev. C 61 (2000) 034607.
[13] Y. Yariv, Z. Fraenkel, Phys. Rev. C 20 (1979) 2227.
[14] W.A. Friedman, et al., MSU preprint MSUCL-1167, July 2000, Phys. Rev. C 62 (2000) 064609.
[15] D.J. Morrissey, B.M. Sherrill, Philos. Trans. Roy. Soc. London A 356 (1998) 1985.
[16] Y.P. Viyogi, et al., Phys. Rev. Lett. 42 (1979) 33.
[17] A.S. Goldhaber, Phys. Lett. B 53 (1974) 306.
[18] R. Dayras, et al., Nucl. Phys. A 460 (1986) 299.
[19] K. Van Bibber, et al., Phys. Rev. Lett. 43 (1979) 840.
[20] D.J. Morrissey, Phys. Rev. C 39 (1989) 460.
[21] W.A. Friedman, Phys. Rev. C 27 (1983) 569.
[22] O. Tarasov, in preparation; also available at http://www.nscl.msu.edu/lise/up.html.
[23] V. Borrel, et al., Z. Phys. A 314 (1983) 191.
[24] F. Rami, et al., Nucl. Phys. A 444 (1985) 349.
[25] N. Iwasa, et al., Nucl. Instr. and Meth. B 126 (1997) 284.
[26] D. Bazin, B. Sherrill, Phys. Rev. E 50 (1994) 4017.
[27] K.L. Brown, D.C. Carey, C. Iselin, F. Rothacker, Transport: a computer program for designing charged particles beam transport systems, CERN 80-04, 1980.
[28] F. Hubert, R. Bimbot, H. Gauvin, Atom. Data Nucl. Data Tables 46 (1990) 1.
[29] L.C. Northcliffe, R.F. Schilling, Nucl. Data Tables A 7 (1970) 233.
[30] J.F. Ziegler, et al., The Stopping and Range of Ions in Solids, Pergamon Press, New York, 1985.
[31] D. Guillemaud-Mueller, M.O. Lampert, D. Pons, M. Langevin, IEEE Trans. Nucl. Sci. 33 (1) (1986) 343.
[32] R. Anne, et al., Nucl. Instr. and Meth. B 34 (1988) 295.
[33] J.A. Winger, B.M. Sherrill, D.J. Morrissey, Nucl. Instr. and Meth. B 70 (1992) 380.
[34] A. Leon, et al., Atom. Data Nucl. Data Tables 69 (1998) 217.
[35] K. Shima, T. Ishihara, T. Mikumo, Nucl. Instr. and Meth. 200 (1982) 605.
[36] G. Audi, A.H. Wapstra, Nucl. Phys. A 595 (1995) 409.
[37] G. Audi, A.H. Wapstra, Nucl. Phys. A 565 (1993) 1.
[38] G. Pfennig, H. Klewe-Nebenius, W. Seelmann-Eggeberg, Chart of the Nuclides, Sixth Edition, 1995, printed by Druckhaus, Haberbeck GmbH, D-32791 Lage/Lippe.
[39] J.K. Tuli, Brookhaven National Laboratory, P.O. Box 5000, Upton, NY 11973-5000, USA.
[40] J.M. Daugas, et al., Phys. Lett. B 476 (2000) 213.
[41] B. Blank, et al., Phys. Rev. Lett. 84 (2000) 1116.